An Investigation into the Validation of Numerical Solutions of Complex Flowfields

Z. Jiang and K. Takayama

Shock Wave Research Center, Institute of Fluid Science, Tohoku University,
2-1-1 Katahira, Aoba-ku, Sendai 980-8577, Japan
E-mail: jiang@ifs.tohoku.ac.jp and takayama@ifs.tohoku.ac.jp

Three cases, including a two-dimensional, an axisymmetric, and a three-dimensional flowfield, were studied to demonstrate the effectiveness and reliability of a method proposed for validation of numerical solutions of complex flowfields. Images of these flowfields were first constructed from numerical solutions based on the principle of experimental flow visualization, and then compared directly with experimental interferograms. Because both experimental and numerical results are of identical physical representation, agreement between them can be evaluated effectively by examining characteristic flow structures of the flowfields as well as comparing differences in density. An efficient algorithm for three-dimensional density integration was also proposed to replace the conventional one that is computationally expensive. The study shows that reliable validation can be achieved in this way because it allows a direct comparison between numerical and experiment results without any loss of accuracy in either of them. The validation method is highly recommended for three-dimensional flowfields where quantification of images from experimental flow visualization is very difficult or impossible. ©c 1999 Academic Press

Key Words: CFD validation; numerical visualization; holographic interferogram; three-dimensional density integration.

1. INTRODUCTION

The recent progress in the computational fluid dynamics has made it possible to simulate various complex three-dimensional flowfields including many shock waves. This progress strengthens our ability to highlight physics in flowfields that are difficult to clearly visualize experimentally. However, it becomes increasingly important to validate these numerical solutions before relying on them to explain the physics of the flowfields. This is necessary because the modeling of physical phenomena often induces some simplifications in

both governing equations and boundary conditions. Furthermore, to a certain extent, the numerical algorithms are only approximations of these governing equations. Therefore, the resulting numerical solutions may or may not represent the real flowfield being considered. In addition, good agreement between numerical and experimental results is necessary to confirm the phenomena observed from experiments, especially in the visualization of three-dimensional flowfields. For example, the widely used holographic interferometry produces only integral views of three-dimensional flowfields by recording the light phase shift due to density variations [19]. Hence the phenomena observed from such images are not very easily interpreted.

The validation of numerical solutions has been carried out for decades and usually was done by comparing them with exact solutions or experimental measurements at some measurement stations in flowfields. However, in recent research work, most of the flowfields under study are highly transient, such as shock wave reflection, diffraction, and interaction, for which there are no exact solutions. Moreover, characteristic flow structures of interest may occupy the whole flowfield. It is therefore usually not sufficient to compare numerical solutions with a limited set of point measurements from experiments. Only through a comparison with the data from the whole flowfield measured by non-intrusive techniques can confidence in numerical solutions be established. From this point of view the validation has two aspects: one is a check on numerical values and the other is a check on characteristic flow structures. Such a validation is still a challenging problem in the Computational Fluid Dynamics (CFD) of complex flowfields.

There are several ways in which experimental flow visualization has been applied to the validation of numerical solutions. The most widely used method for two-dimensional flows displays numerical results in the form of isopycnics which can be compared with experimental infinite-fringe interferograms (for example, Sasoh *et al.* [12], Inoue *et al.* [4], Sun and Takayama [13], and Takayama and Jiang [15]). The comparison in this way is quite informative since the interferometric fringes in the case of two-dimensional flows give an indication of density contours. However, the evaluation of accuracy is not easy to make because the corresponding position of numerical isopycnics within fringes is difficult to locate accurately. Furthermore, in the case of axisymmetric or three-dimensional flows, the evaluation becomes even more difficult because the fringes no longer correspond to contours of density, which is averaged along the light path. Using numerical results as initial values on boundaries to count fringes, Sun and Takayama [13] reported a quantitative image analysis of infinite-fringe interferograms to validate their numerical solutions. Useful comparison can be made with this technique but the accuracy varies with the method used to locate isopycnics within fringes. Finite-fringe interferograms can also be analyzed with image processing techniques, as reported by Havener and Obergefell [3] and Jiang *et al.* [5]. More data are readily available using their methods but the loss of accuracy in experimental data cannot be avoided. This is because each fringe is broadened to a certain width and the data are available only at the fringes. So, these methods must use a linear interpolation between fringes to obtain more data, which leads to errors in highly non-linear flowfields. Fourier transform fringe analysis supplies more information with high accuracy but is limited when the hetrodyning frequency of the finite-fringe interferograms is low, as discussed by Babinsky and Takayama [2]. However, all of the above-mentioned methods are of limited use for three-dimensional unsteady flows. A tomographic reconstruction method can be used to obtain density information but it is experimentally intensive because one projection is insufficient to determine density distribution and several tens of density

projections from different viewing directions must be provided simultaneously (Taketa *et al.* [16]; Parker [9], and Morton *et al.* [10]). Considering the above discussion, the strategy of creating numerical interferograms for direct comparison with experiments was discussed for CFD validation by many authors (Havener and Obergefell [3], Tamura and Fujii [18], Tam *et al.* [17], Yates [20], Babinsky *et al.* [1], and Jiang *et al.* [7, 8]). From the number of fringes and their distributions, the accuracy of numerical values and agreement on characteristic flow structures appearing in the results can be estimated.

In the present study, three cases of two-dimensional, axisymmetric, and three-dimensional flowfields were investigated to explore further ways to CFD validation through a direct comparison between numerical and experimental results. Various aspects of this validation and the techniques used in the image processing are discussed in detail, especially for the latter two cases. The algorithm for integrating density in axisymmetric flowfields was described by Havener and Obergefell [3] and three-dimensional density integration was performed by Yates [20]. In this paper, an efficient algorithm for integrating three-dimensional density distributions was developed to replace the one previously used by Yates [20]. The new algorithm is much faster and will make the three-dimensional post-processing more widely applicable. The study shows that creating a direct comparison is a promising way to approach reliable CFD validation, especially for three-dimensional flowfields where density-integrated effects make experimental images very difficult to interpret.

2. PRINCIPLE OF OPTICAL FLOW VISUALIZATION

Interferometry, schlieren, and shadowgraph are three techniques widely used in optical flow visualization. These optical techniques use the principle that as light passes through a flowfield its phase and direction are changed due to variations of the refractive index induced by non-uniform density in the flowfield. This makes it possible to analyze physical phenomena that manifest themselves as density changes in the flowfields. Discussions on the above techniques appear in numerous text books and in the literature. A brief summary is given here for completeness.

In the case of ideal and non-reacting gases, the refractive index n is related to the density ρ by the Gladstone–Dale equation.

$$n(x, y, z) = 1 + K_g \rho(x, y, z), \tag{1}$$

where K_g is the Gladstone–Dale constant that changes depending upon gas species and varies slightly with the light wavelength. In holographic interferometry, double exposure interferograms are generated by exposing the film to the object and the reference beam. For infinite-fringe interferometry, the object beam passes through the flowfield, and its phase changes due to variations of the refractive index caused by density changes between exposures but the reference beam does not change. The phase shift of the object beam relative to the reference beam between exposures is calculated by integrating

$$\Delta\phi(x_{im}, y_{im}) = \frac{2\pi}{\lambda} K_g \int_0^{L_0} (\rho(x, y, z) - \rho_0) \, dl, \tag{2}$$

where λ is the wavelength of the light, ρ_0 the density of the undisturbed flow, and L_0 the length of the light path through the test section. The image intensity of the infinite-fringe

interferograms I can be calculated by

$$I = 1 + \cos(\Delta\phi(x_{im}, y_{im}) + \phi_0), \tag{3}$$

where (x_{im}, y_{im}) denotes the image plane and ϕ_0 is an initial phase shift to compensate for any phase shift between two exposures and is taken as zero in most of the cases. The fringe shift N is given by

$$N = \frac{1}{2\pi}\Delta\phi(x_{im}, y_{im}). \tag{4}$$

This corresponds to the fringe number in infinite-fringe interferograms. Integrating density along the actual light path as the light deflects through the flowfield in the test section should be carried out by using Eq. (2), but the procedure is computationally expensive. The straight line approximation is accepted in the present work [20], which was proven to be a good approximation when the test section is not too big and the density change is not too large.

In the case of finite-fringe interferograms achieved by tilting the reference beam between exposures, the image intensity is given by

$$I = 1 + \cos(\Delta\phi(x_{im}, y_{im}) + 2\pi v_x x_{im} + 2\pi v_y y_{im}), \tag{5}$$

where v_x and v_y are the special frequency components of the unperturbed fringes.

The schlieren method is also a very popular flow visualization technique. The intensity of each point in schlieren photographs is proportional to the density gradient perpendicular to the knife edge because the ray deflection is proportional to the density gradient. When the knife is set to be perpendicular to the x-axis in the physical space the intensity I is proportional to the integration of the density gradient along the ray.

$$I \propto \int_0^{L_0} \frac{\partial \rho(x, y, z)}{\partial x} \, dl. \tag{6}$$

Shadowgrams are also widely used in aerodynamic experiments. For these, the image intensity is proportional to the gradient of the integration of grad $\rho(x, y, z)$ in the direction perpendicular to the light ray, which can be calculated by

$$I \propto \text{grad} \int_0^{L_0} \text{grad } \rho(x, y, z) \, dl. \tag{7}$$

Since both the schlieren and shadowgraph methods can provide only qualitative information, these methods are not used as frequently as interferometry in applications to the CFD validation.

3. SHOCK WAVE REFLECTION OVER A WEDGE: A TWO-DIMENSIONAL CASE

We now consider the two-dimensional case of shock wave reflection over a wedge. The optical setup is schematically shown in Fig. 1. In this setup, the light beam is split into two and collimated with two collimating mirrors: one of these beams is chosen as the reference beam and the other as the object beam. The reference beam and the object beam are then superimposed on a holo-film by means of two reflecting mirrors.
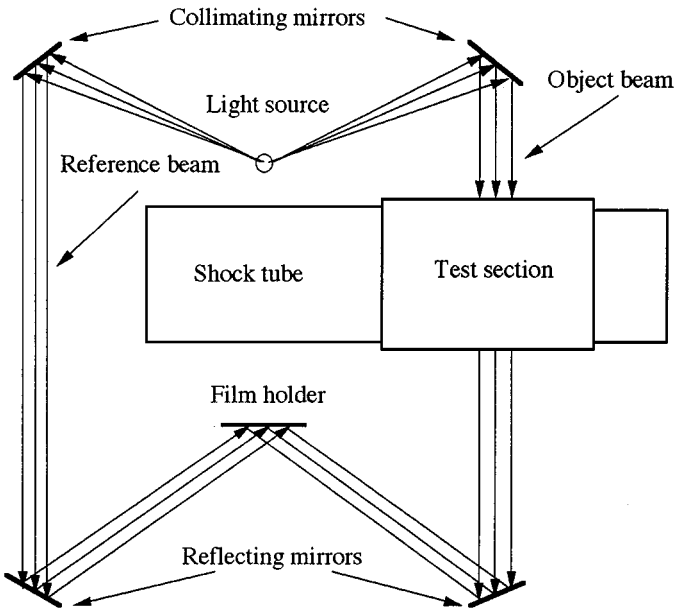
FIG. 1. Schematic for constructing two-dimensional interferograms.

In a two-dimensional case, density distributions on planes perpendicular to the light ray within a test section are identical so that the equation of (2) is simply reduced to

$$\Delta\phi(x_{im}, y_{im}) = \frac{2\pi}{\lambda} K_g L_0 (\rho(x_{im}, y_{im}) - \rho_0), \tag{8}$$

where the image plane is parallel to the computational plane and L_0 is the width of the test section.

This test case is a shock wave reflection over a $46°$ wedge for $M_i = 2.0$ and is numerically simulated by solving the Euler equations with a dispersion-controlled scheme proposed by Jiang *et al.* [6]. The numerically determined density is processed to produce a synthetic interferogram by using Eq. (8) and the resulting image is shown in Fig. 2. The experimental interferogram obtained by using holographic interferometry is shown in Fig. 3. A schlieren photograph computed by using Eq. (6) and isopycnics plotted with the same density data are shown in Figs. 4 and 5, respectively.

By comparing Figs. 2 with 3 it can be observed that the number of fringes in these two photographs is the same, the length of the Mach stem is identical, and fringe distributions coincide with each other. Therefore, good agreement between them can be concluded. Minor discrepancies exist near the wedge tip and the contact surface from the triple point. These discrepancies can be recognized to be due to the wedge difference between the CFD simulation and the experiment, and the effect of viscosity. From this comparison, agreement or disagreement on shock wave structures can be recognized readily and the factor contributing to disagreement can be easily deduced. Such a comparison is very important for shock wave research since shock wave structures are specially emphasized in this way. In addition, the validation shows that the equations solved in this case are correct for the study of shock-wave reflection but not so for the investigation into shear layer development.
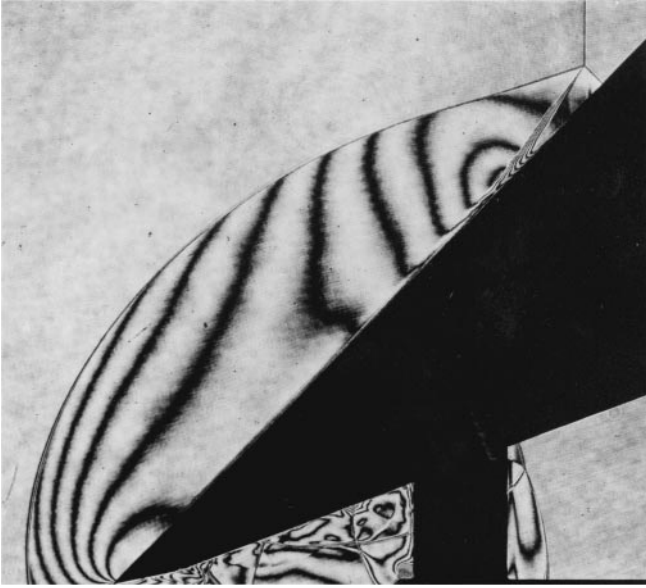
FIG. 2. Experimental interferogram of shock wave reflection over a 46° wedge for $M_i = 2.0$.

Quantitative validation is also available in this case by quantifying the experimental interferogram. Since the actual level of density shift between fringes is known, counting the number of fringes between the location of known density and the point of interest provides quantitative density information [13]. However, the positions of specific isopycnics such as those in Fig. 4 are not easily determined from the experimental interferogram as shown in Fig. 2. It is usually assumed that the middle line of each fringe is the position of the corresponding isopycnics. Unfortunately, this will introduce errors because the flowfields
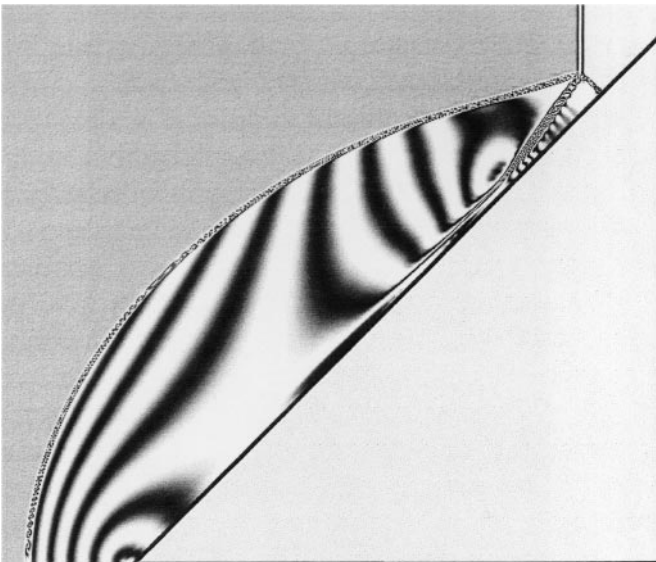

FIG. 3. Numerical interferogram of shock wave reflection over a 46° wedge for $M_i = 2.0$.
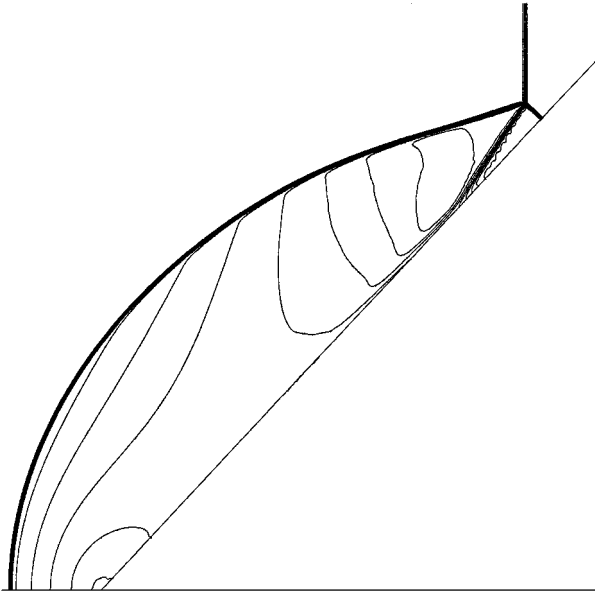
FIG. 4. Isopycnics of shock wave reflection over a $46°$ wedge for $M_i = 2.0$.

are highly non-linear in most of the cases of interest. One of the advanced techniques is Fourier transform fringe analysis. This is applied to finite-fringe interferograms to obtain actual density of flowfield with error levels among fractions of the density difference between two fringes [16]. However, if the density jump across a shock wave is larger than the density difference between two fringes, the relevant area of the flowfield is very difficult to quantify. In that case, a phase-unwrapping algorithm is required to determine the correct fringe shift. However, such an algorithm will not work if the shock waves are everywhere strong [21],
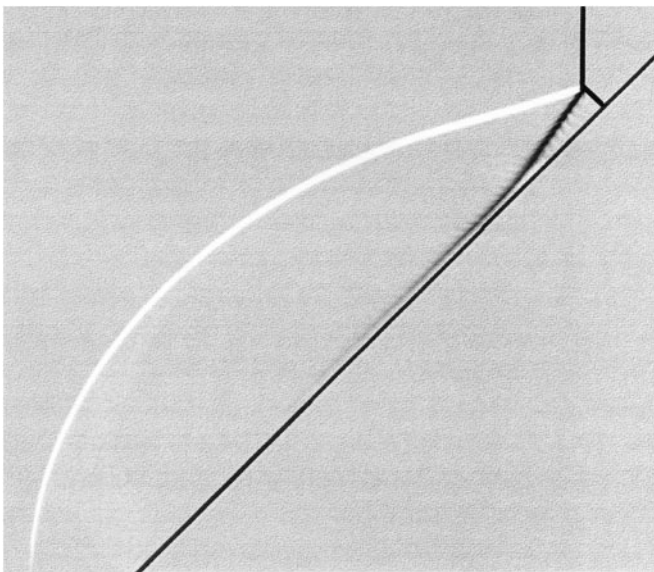

FIG. 5. Numerical schlieren of shock wave reflection over a $46°$ wedge for $M_i = 2.0$.

since it requires a starting point where the magnitude of the fringe shift is less than one. In conclusion, these quantifying methods are very useful in practice but will result in a loss of accuracy to a certain extent or will be limited to some special cases. It seems that the comparison done above makes the best use of the experimental data.

Figure 5 shows a schlieren photograph of the shock wave reflection. Features related to sharp discontinuities in density, such as shock waves, the Mach stem, and the contact surface, are easily visualized against the background but continuous density distributions are poorly visualized. Shadowgrams also show similar characters of the flowfield. Therefore, for quantitative validation of numerical solutions the interferogram is preferable.

4. SHOCK WAVE PROPAGATION IN A TUBE WITH SUDDEN AREA CHANGE: AN AXISYMMETRICAL CASE

In the case of axisymmetric flows the principle for constructing interferograms under the assumption of the straight line approximation is schematically shown in Fig. 6. Here the reference beam and the object beam are still superimposed on the holo-film but the density distribution on the planes perpendicular to the light ray within the test section varies along the light path. Considering this difference and the symmetry of the physical domain, the phase shift expressed by Eq. (2) can be calculated by Eq. (9) when the light path is perpendicular to the axis of symmetry,

$$\Delta\phi(x_{im}, y_{im}) = \frac{4\pi}{\lambda} K_g \int_{y_{im}}^{R} (\rho(x, r) - \rho_0) \, dr, \tag{9}$$

where R is the diameter of the physical domain and the integration is performed from $r = y_{im}$ to $r = R$ along the light path. This integration is not as straightforward as that in
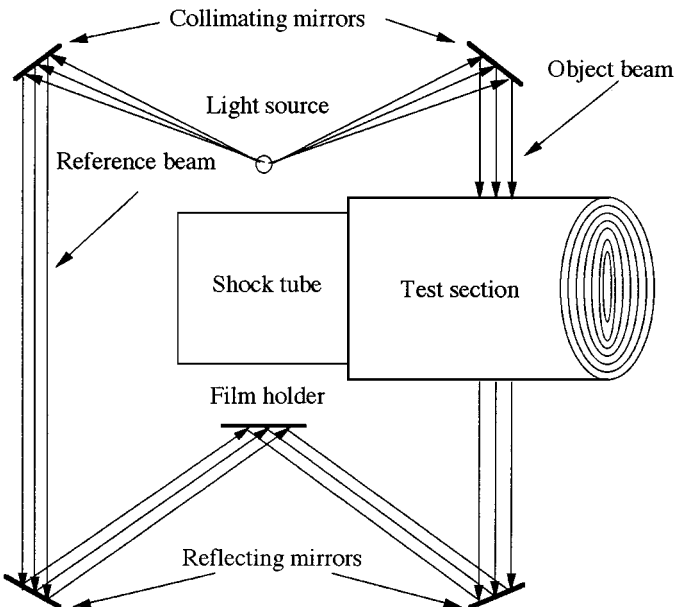

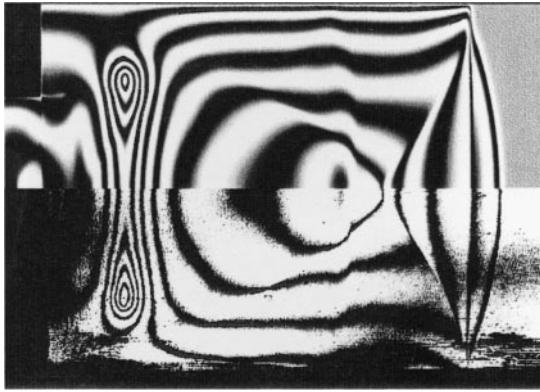**FIG. 6.** Schematic for constructing axisymmetrical interferograms.

FIG. 7. Numerical (the upper half) and experimental (the lower half) interferogram at an early stage of shock wave propagation for $M_i = 1.3$.

two-dimensional cases but is still quite simple to calculate. A more detailed description of the density integration was given by Havener and Obergefell [3]. For this second test case, shock wave propagation in a tube with a sudden area change in its cross section (a large-diameter chamber is connected to a small-diameter shock tube) is simulated by using the same numerical code as that used for the first case. The Mach number is taken to be $M_i = 1.3$ and the ratio of the diameter of the large chamber to the diameter of the shock tube is taken as $2 : 1$. This large chamber is specially designed to have an aspheric cross section which allows the collimated incident ray to traverse the transparent wall of the test section parallel, and to emerge parallel. A detailed description of the experiment was given by Takayama and Onodera [14] and Jiang *et al.* [7]. A combination of experimental and numerical interferograms of the flowfield at an early stage is shown in Fig. 7 and that at a later stage is shown in Fig. 8. Isopycnics of numerical solutions in the symmetric plane at the later stage are shown in Fig. 9.

As is expected, the difference between the interferogram shown in Fig. 8 and the numerical isopycnics shown in Fig. 9 is obvious because of the axisymmetric density distribution. The
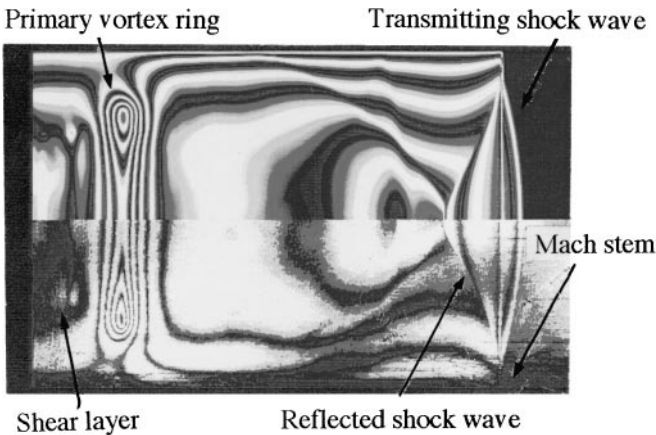

FIG. 8. Numerical (the upper half) and experimental (the lower half) interferogram at a later stage of shock wave propagation for $M_i = 1.3$.
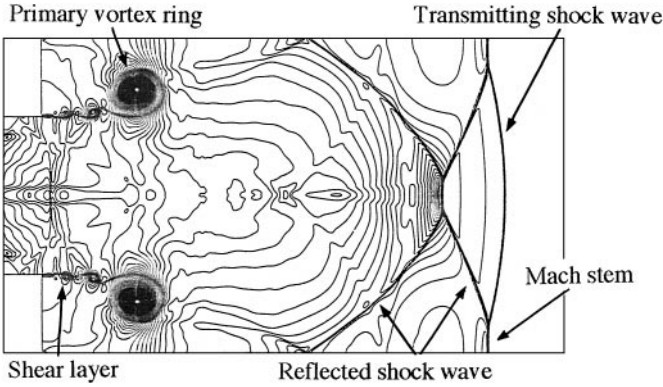
FIG. 9. Numerical isopycnics at a later stage of shock wave propagation for $M_i = 1.3$.

transmitting shock wave, the primary vortex ring, and the shear layer appear in different ways in these two kinds of displays. Furthermore, the shock wave reflection from the tube wall is clearly visible in the isopycnics, but is smeared in the interferogram due to the effects of the integral view. Hence the physical understanding of the wave phenomena is less easy to reach and conclusions about the CFD validation are difficult to draw. However, if the validation strategy is changed by constructing a numerical interferogram, as shown in the upper halves of Figs. 7 and 8, to compare them with the corresponding experimental ones, as shown in the lower halves of these figures, it is readily observed that agreement between the numerical and the experimental interferogram is excellent. This indicates that comparison of numerical and experimental results is easier when two results are displayed based on the same principle. In such circumstances, we can reach a conclusion much more easily and avoid misinterpretation.

Validation of unsteady-state flowfields is also demonstrated by this case. The interferograms shown in Figs. 7 and 8 represent two successive stages of the shock wave propagation. Good agreement between these two pairs of interferograms implies that the CFD validation of the unsteady-state flows can be done without any problem provided that the experimental facility can produce images of the flowfields with a high degree of repeatability.

Further validation can be explained with Figs. 7 and 8. From these figures, the deviation of each fringe in the upper half (the numerical data) from the corresponding one in the lower half can be determined so that the accuracy of the integrated density of the numerical results can be estimated. For instance, the maximum shift in fringe positions observed in Fig. 8 is less than 10% of the interval between neighboring fringes. Because one fringe shift indicates that the density change is 13.68% of the initial density in front of the transmitting shock wave, this maximum discrepancy means that the difference in the integrated density is less than 1.4% of the initial density according to fringe pattern analysis. This implies that the accuracy level reached could be as high as that obtained by quantifying the experimental interferogram with Fourier transform fringe analysis.

It is also necessary to point out that perturbations in the test section may make experimental fringes move slightly forward or backward so that the experimental uncertainty imposes more difficulties on estimating accuracy of numerical solutions. Moreover, the difficulty in timing numerical results to match exactly with experiments also results in fringe shift between the numerical image and the experiment. Therefore, the level of validation

achieved in the comparison described above is an acceptable way to show that the numerical simulations represent the shock wave flow.

In addition, evaluation of the validation also depends on the purpose of the study. For example, if the shock wave motion and shock wave interaction are emphasized in this case, the agreement concluded from the comparison is excellent. However, if shock-wave/boundary-layer interaction is to be investigated, it is obvious that this is not so, because the boundary layer is not visible in the experimental results due to experimental limitations, and the numerical solutions are only based on the Euler equations.

Quantification of the axisymmetric interferogram is possible by performing an inverse transformation of the integrated image data to obtain the density information on the symmetric plane. However, the computational process may break down and the accuracy of the numerical value may be compromised in the case of flowfields with many strong shock waves. We therefore conclude that the validation for the axisymmetric case is more efficient and easy to carry out as described above.

5. TRANSMITTING SHOCK WAVE DISCHARGED FROM A SQUARE TUBE: A THREE-DIMENSIONAL CASE

For three-dimensional flowfields, the reconstruction of density from interferograms is theoretically possible with the use of tomographic techniques, which allows an unknown density distribution to be determined from line integrals of optical density through the distribution. However, in order to perform the inversion successfully, several tens of interferograms in different viewing directions at the same time must be provided for complex flowfields [9, 10]. As imagined, tomographic inversion is immensely difficult in highly unsteady flows because recording many flow images simultaneously is extremely difficult to achieve. In comparison, creating computational interferograms from the three-dimensional density distribution is more feasible for CFD validation. In three-dimensional cases, the density integration expressed by Eq. (2) requires expensive image processing. In the following subsection, an efficient algorithm for integrating the density is described. In addition, interferograms, generated with the algorithm, will be compared with experiments to demonstrate the feasibility of the three-dimensional CFD validation and the efficiency of the proposed algorithm.

5.1. An Efficient Algorithm for Three-Dimensional Density Integrations

A schematic for integrating the three-dimensional density with the previously used method [20] is shown in Fig. 10, where the interval $x_j \leq x_{j+1}$ defines the intersection of the light path with a computational cell. Tracing the light path as it passes through the flowfield and integrating the appropriate function of the refractive index along this path are computationally expensive even if the straight line approximation is used. In this process it is necessary to determine the computational cell that the light intersects with, find the intersected points on the computational cell, interpolate the density at these two points, and calculate the integral for this segment and add it to the appropriate sum. The first three of these operations are the most time consuming for the density integration. To overcome this difficulty and make the three-dimensional post-processing more efficient, a fast algorithm is proposed in this paper and described in detail in the following.

It is assumed that there is a known density of the flowfield, defined by $[0, X] \times [0, Y] \times [0, Z]$ and divided into equal mesh sizes, Δx, Δy, and Δx, in the x-, y-, and z-directions,
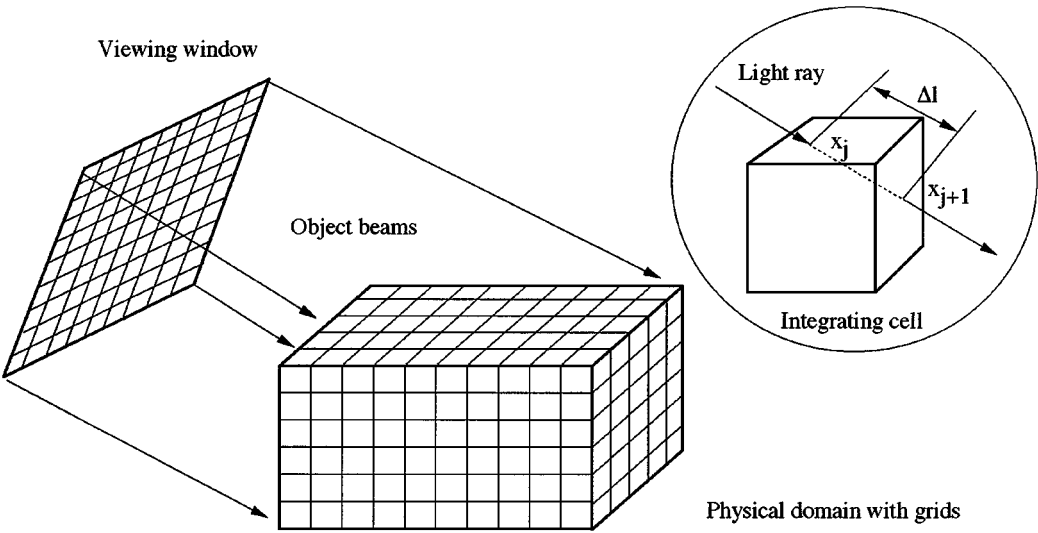
FIG. 10.   Schematic for three-dimensional density integration.

respectively. This is defined as the physical domain, as shown in Fig. 10. The angles of the viewing direction with respect to three coordinate axes are denoted by α, β, and γ, respectively, as shown in Fig. 11. Of these angles, α is the smallest. Therefore, the x-direction is chosen as the main viewing direction. The image plane is then created and defined by $[0, Y_{im}] \times [0, Z_{im}]$, and also equally spaced with arbitrary grid sizes. For density integration, an integrating domain (x', y', z') is set up with its centroid located at point $(X/2, Y/2, Z/2)$ (see Fig. 11), and its length, width, and height are taken as L, W, and H, respectively. $Y_{im} = W$ and $Z_{im} = H$ are kept between the image plane and the integrating domain. These three parameters are estimated approximately by
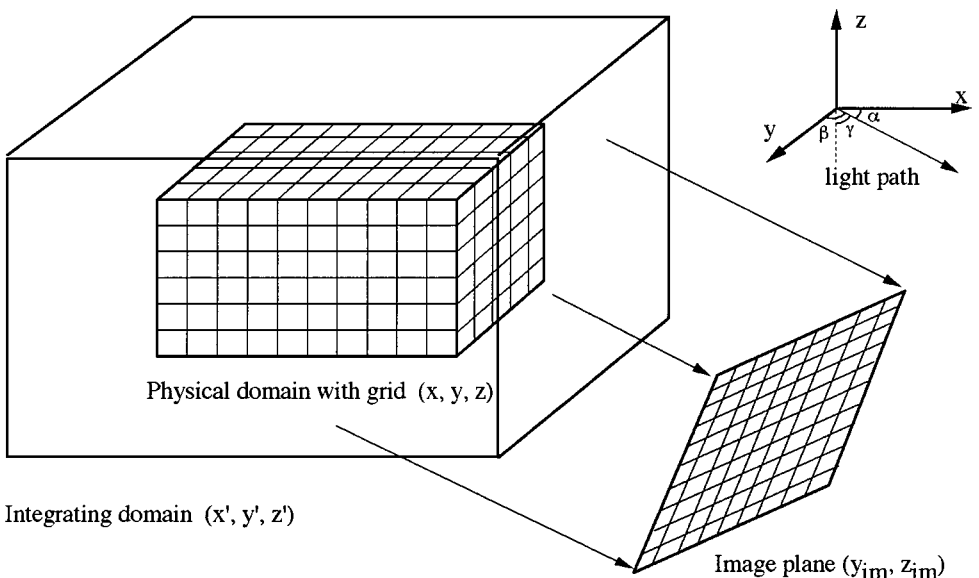

FIG. 11.   Schematic for coordinate transformation.

$$\begin{cases} L = X \cos\alpha + Y \sin\beta + Z \sin\gamma \\ W = X \sin\alpha + Y \cos\beta + Z \sin\gamma \\ H = X \sin\alpha + Y \sin\beta + Z \cos\gamma. \end{cases} \quad (10)$$

The size of the integrating domain is deliberately determined so that it still contains the whole physical domain after this domain is rotated around its centroid at the angle (α, β, γ).

The integrating domain is then rotated around its centroid in the angles of the viewing direction (α, β, γ) so that the grid lines in the x'-direction are parallel to the light ray. The coordinates for the eight corners of the integrating domain are calculated by

$$\begin{cases} x'_i = r \cos(\alpha_i + \alpha) + X/2, \\ y'_i = r \cos(\beta_i + \beta) + Y/2, \qquad i = 1, \ldots, 8 \\ z'_i = r \cos(\gamma_i + \gamma) + Z/2, \end{cases} \quad (11)$$

with

$$\begin{cases} r = [(x_i - X/2)^2 + (y_i - Y/2)^2 + (z_i - Z/2)^2]^{1/2} \\ \alpha_i = \arccos[(x_i - X/2)/r]^2 \\ \beta_i = \arccos[(y_i - Y/2)/r]^2 \\ \gamma_i = \arccos[(z_i - Z/2)/r]^2. \end{cases} \quad (12)$$

Once the coordinates for these eight corner points are known the internal points of the integrating domain can be calculated easily because only an equally spaced grid is required. The process costs very little CPU time.

The next step is to interpolate the density at each point in the integrating domain from the physical one. First, all grid points in the integrating domain are divided into two classes. If the point, $P(x', y', z')$, is out of the physical domain the density at it is set to be ρ_0 so that there will be no contribution from it to density integration by using Eq. (2). If this point falls into the physical domain it is necessary to count its contribution. To do so, the cell containing this point in the physical domain must be found. For the case described above it is simply identified by calculating the index number of the lowest corner of the cell.

$$\begin{cases} i = \mathrm{Int}(x'/\Delta x) \\ j = \mathrm{Int}(y'/\Delta y) \\ k = \mathrm{Int}(z'/\Delta z). \end{cases} \quad (13)$$

To simplify the density interpolation, a new local coordinate is set up with its origin at $P(x'_i, y'_j, z'_k)$. The local coordinates for the point, $P(x', y', z')$, are expressed by

$$\begin{cases} \xi = (x' - x'_i)/\Delta x \\ \eta = (y' - y'_j)/\Delta y \\ \zeta = (z' - z'_k)/\Delta z. \end{cases} \quad (14)$$

The density interpolation can be carried out as follows,

$$\begin{aligned} \rho(x', y', z') = {} & N_{i,j,k}\rho_{i,j,k} + N_{i+1,j,k}\rho_{i+1,j,k} + N_{i,j+1,k}\rho_{i,j+1,k} \\ & + N_{i+1,j+1,k}\rho_{i+1,j+1,k} + N_{i,j,k+1}\rho_{i,j,k+1} + N_{i+1,j,k+1}\rho_{i+1,j,k+1} \\ & + N_{i,j+1,k+1}\rho_{i,j+1,k+1} + N_{i+1,j+1,k+1}\rho_{i+1,j+1,k+1} \end{aligned} \quad (15)$$

with

$$
\begin{cases}
N_{i,j,k} = (1 - \xi)(1 - \eta)(1 - \zeta) \\
N_{i+1,j,k} = \xi(1 - \eta)(1 - \zeta) \\
N_{i,j+1,k} = (1 - \xi)\eta(1 - \zeta) \\
N_{i+1,j+1,k} = \xi\eta(1 - \zeta) \\
N_{i,j,k+1} = (1 - \xi)(1 - \eta)\zeta \\
N_{i+1,j,k+1} = \xi(1 - \eta)\zeta \\
N_{i,j+1,k+1} = (1 - \xi)\eta\zeta \\
N_{i+1,j+1,k+1} = \xi\eta\zeta.
\end{cases}
\tag{16}
$$

Once the interpolation is done, density integration starting from each point in the image plane is simply expressed by a sum of density values at grid points along grid lines in the x'-direction.

$$
\Delta\phi(y_j, z_k) = \frac{2\pi}{\lambda} K_g \Delta x' \sum_{i=1}^{N_I} [\rho(x_i', y_j', z_k') - \rho_0] \qquad \text{for all } (j, k) \in ID, \tag{17}
$$

where ID stands for the image domain, and N_I is the total number of grid points in the x'-direction of the integrating domain with a mesh size of $\Delta x'$. The interpolating process is greatly simplified with these equations and the resulting computer code can be perfectly vectorized because it is not necessary to judge whether a cell intersects with the light path or not. As a result of the improvement, the newly developed code is about 20 times faster that the one based on the conventional integrating algorithm [20].

5.2. *Comparison of Numerical and Experimental Results*

The third test case is shock wave diffraction, created by discharging a transmitting shock wave from the open end of a square shock tube into ambient air for a shock Mach number of 1.5. The shock wave at the open end is initially planar, but it quickly develops into a spherical shape via a three-dimensional transition with time. The diffraction of the shock wave was visualized from three viewing directions as defined in Fig. 12. The first viewing direction is normal to the side walls and is named the side view. For comparison, the plane
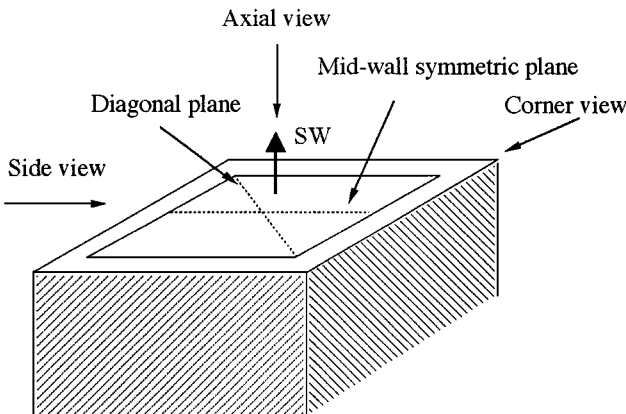

FIG. 12. Geometry and viewing directions.

crossing the middle of the side walls and normal to this view direction is called the mid-wall symmetrical plane. The second view direction is along the diagonals that cross two corners of the shock tube and is referred to as the corner view. The plane normal to this viewing direction and crossing the diagonals is called the diagonal plane. The last one is along the axis of symmetry and is defined as the axial view.

The three-dimensional hyperbolic system of the conservation laws for a perfect gas was solved using a dispersion-controlled scheme [6] on an equally spaced grid with $200 \times 150 \times 150$ mesh points. Experiments were conducted in a 40×40 mm square cross-sectional tube connected to a 60×150 mm diaphragmless shock tube in the Shock Wave Research Center, Tohoku University, Japan [19]. The diffraction of the shock wave was visualized with double exposure holographic interferometry. Both numerical and experimental results viewed in three viewing directions are shown in Figs. 13 to 15, respectively. Figure 13 shows side views of shock wave diffraction, Fig. 14 shows the corner views, and Fig. 15 shows the axial view viewed from 15° degree off the axis of symmetry. The isopycnics on both the mid-wall symmetric and the diagonal planes are also plotted in Fig. 16.

Carefully examining each pair of interferograms shown in Figs. 13 to 15, one sees that agreement between the numerical and experimental results is good: the number of fringes and their distributions coincide very well with each other. The only discrepancy between
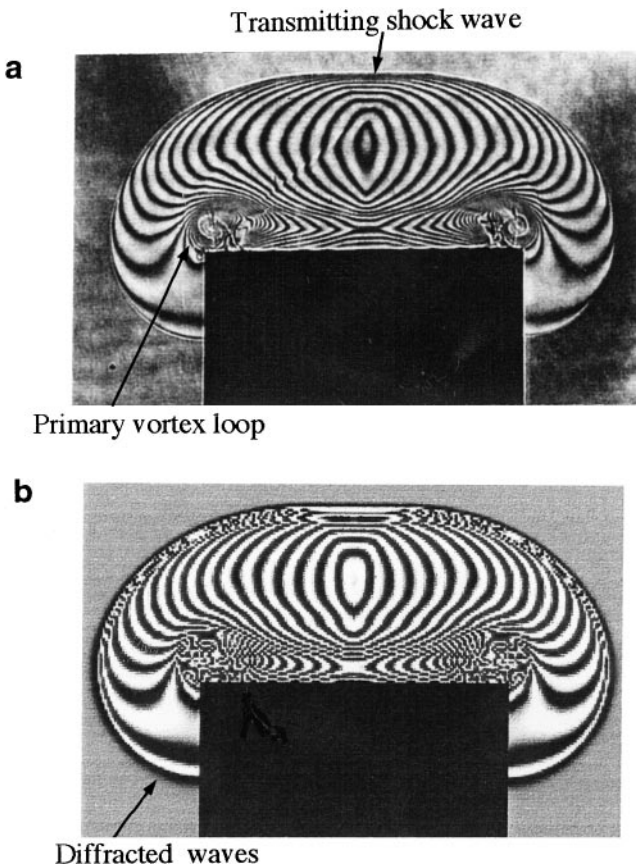

FIG. 13. Side views of three-dimensional shock wave diffraction for $M_i = 1.5$. (a) Experimental interferogram. (b) Numerical interferogram.
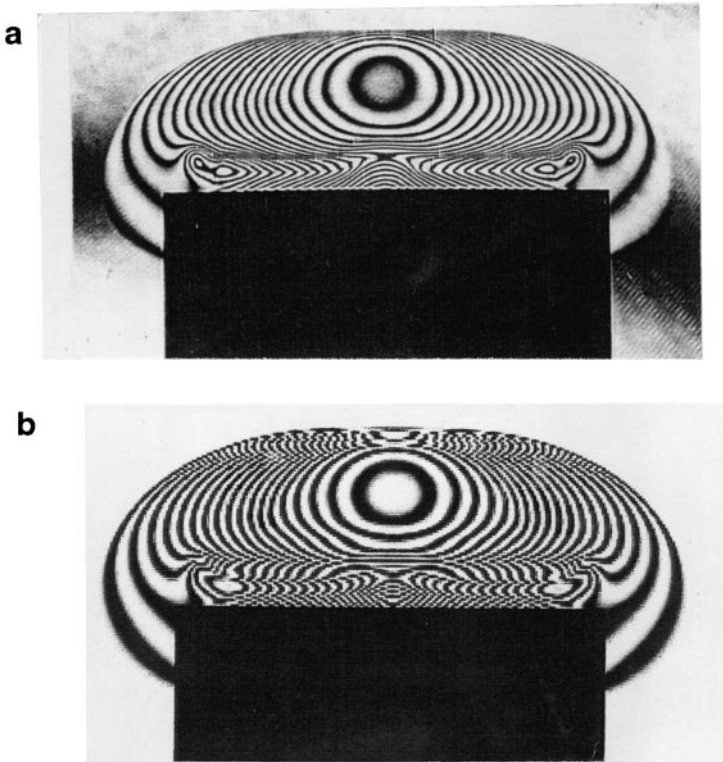
FIG. 14. Corner views of three-dimensional shock wave diffraction for $M_i = 1.5$. (a) Experimental interferogram. (b) Numerical interferogram.

the numerical and experimental interferograms near the exit in Figs. 13b and 14b is due to the fact that the resolution for displaying these numerical images is not fine enough to distinguish as many fringes as are shown in the experimental interferograms in Figs. 13a and 14a, where density gradients are very high. Three pixels, at least, are necessary to visualize one fringe: a dark pixel between two white pixels. If the space between two fringes is smaller than one pixel, computed fringes will be displayed incorrectly. This problem can be avoided when the numerical images are created with somewhat fewer fringes, as shown in Fig. 15. Apart from this minor discrepancy, all the wave phenomena, such as the non-uniform flow expansion created at corners and a secondary shock wave developed near the primary vortex loop, appear to be identical when numerical results are compared with experimental ones. From a comparison of these results obtained by viewing from three viewing directions, it can be concluded that the numerical solutions are well validated.

It is obvious that for the validation of such a complex flowfield, a check on numerical solutions with only a set of point measurements in the flowfield is not sufficient and a comparison between topological flow structures from both numerical and experimental results must be included. Therefore, it may be concluded that good agreement on flow structures implemented with a value check on a few measurement points will provide more acceptable CFD validation.

Comparing Figs. 13 and 14 with 16 reveals some differences between interferometric fringes and numerical isopycnics in both the mid-wall symmetrical and the diagonal plane. Because the fringes in Figs. 13 and 14 represent the integrated density seen by the individual
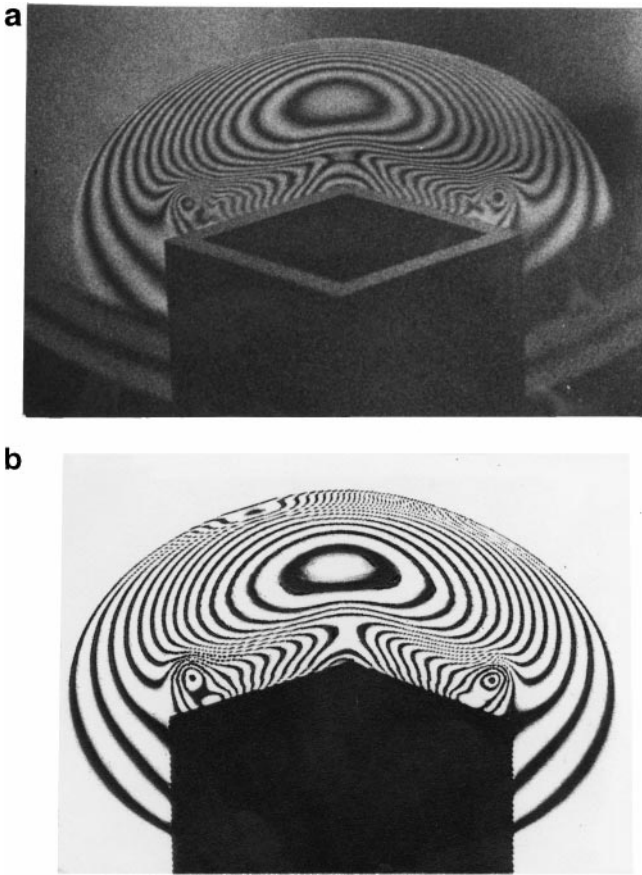
FIG. 15. Axial views of three-dimensional shock wave diffraction for $M_i = 1.5$. (a) Experimental interferogram. (b) Numerical interferogram.

light ray passing through a test section, many planes with different density distributions overlap. This results in many fringes in the central area in the interferograms, as shown in Figs. 13 and 14, but there are no density changes there, as shown in Fig. 16. Moreover, from numerical isopycnics shown in Fig. 16b, the secondary shock wave is clearly observable but is not easily identified from the interferograms shown in Fig. 14. According to the above discussion, it is understood that, for three-dimensional flow visualization, some physical features may appear to be smeared and some non-physical features may be created. Therefore, the experimental data need to be carefully interpreted with reliable numerical results that are capable of showing three-dimensional transient phenomena in detail.

As is well known, both computational fluid dynamics and experimental flow visualization are important tools in the research of fluid science. Because the most interesting problems are three-dimensional and contain transient phenomena, investigations into such flowfields are very important. However, they can be very difficult to conduct. It may be too much to ask experimental flow visualization to provide all the necessary information for understanding these complex flowfields. However, the present study shows that it may be possible to circumvent this difficulty through interferometry provided that the interferograms are clear enough to validate numerical solutions. In other words, experimental images of three-dimensional flowfield need only provide validation of numerical solutions. The
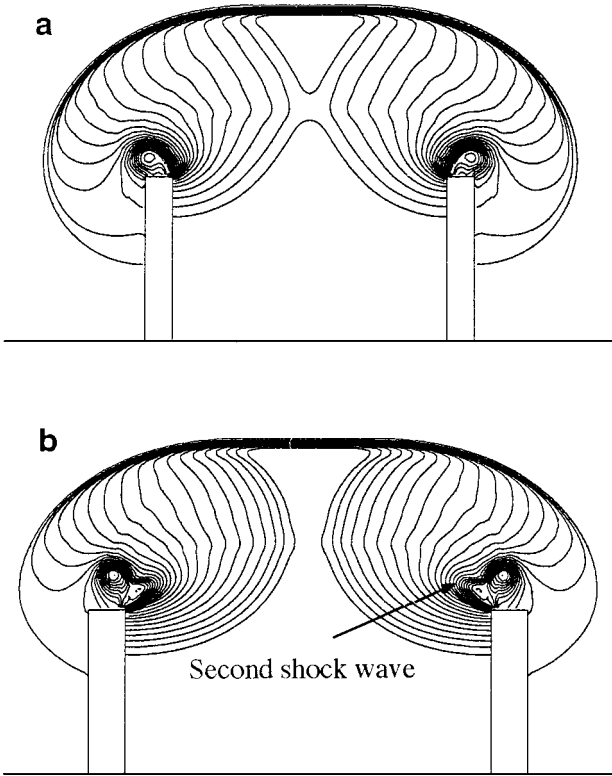
FIG. 16. Isopycnics in two planes of three-dimensional shock wave diffraction for $M_i = 1.5$. (a) The mid-wall symmetric plane. (b) The diagonal plane.

numerical results thus validated, in return, provide some useful information for interpreting complex interferometric patterns. As a result, such a CFD validation works as a tool that combines the CFD and experiments for exploration of the physics that can be done well by neither CFD nor experiments alone.

Finally, in the absence of efficient tomographic reconstruction of the density for three-dimensional complex flows, this direct comparison is a more attractive strategy for whole flowfield validation at an acceptable level of accuracy.

6. CONCLUSIONS

Computational simulation of optical flow visualization can create a direct comparison between numerical and experimental results, and is proven to be a promising way to approach reliable validation of numerical solutions, especially for three-dimensional complex flowfields where quantification of experimental interferograms is almost impossible. This comparison with quantitative characters is an effective approach to whole flowfield validation without any loss of accuracy in either experimental data or numerical results. The proposed algorithm for integrating three-dimensional density works much faster and could make this post-processing technique more widely available. However, in order to achieve reliable validation, the flowfield of interest must be represented correctly by the solved equations, visualized clearly by interferometry, and displayed correctly by computer facilities. In addition, fringe patterns of experimental results in axisymmetric and

three-dimensional flowfields need to be carefully interpreted, taking into account density-integrated effects.

REFERENCES

1. H. Babinsky, T. Meguro, Z. Jiang, and K. Takayama, Numerical visualization of shock wave flow in an expanding tube and comparison with experiment, in *Proc. ASME 1995 on Experimental and Numerical Flow Visualization, Hilton Head, South Carolina, August 13–18, 1995*, edited by Khalighi *et al.*, Vol. 218, p. 89.

2. H. Babinsky and K. Takayama, CFD validation strategies for compressible flow using interferometry, AIAA 96-0438.

3. A. G. Havener and L. A. Obergefell, Computational interferometric description of nested flow fields, *Opt. Engrg.* **24**, 441 (1985).

4. O. Inoue, M. Takahashi, and K. Takayama, Shock wave focusing in a log-spiral dust, *AIAA J.* **31**, 1150 (1993).

5. Z. Jiang, J. Liu, G. Ni, and Y. S. Chen, The calculation of the density field from axisymmetric schlieren interferograms by the image processing techniques, *ACTA Mech. Sinica* **9**, 22 (1993).

6. Z. Jiang, K. Takayama, and Y. S. Chen, Dispersion conditions for non-oscillatory shock capturing schemes and its applications, *Comp. Fluid Dynam. J.* **2**, 137 (1995).

7. Z. Jiang, K. Takayama, H. Babinsky, and T. Meguro, Transient shock wave flows in tubes with a sudden change in cross section, *Shock Waves* **7**, 151 (1997).

8. Z. Jiang, O. Onodera, and K. Takayama, Three-dimensional reflection of shock waves propagating in square cross-sectional tubes, in *Proc. 21st Int. Symp. on Shock Waves, Great Keppel Island, Australia, July 20–25, 1997*, edited by Houwing *et al.*, Vol. 2, p. 1499.

9. S. C. J. Parker, *The Quantitative Analysis of Transonic Flows by Holographic Interferometry*, Ph.D. thesis, University of Warwick, UK (1993).

10. J. W. Morton, A. F. P. Houwing, R. R. Boyce, and D. J. Bone, Tomographic reconstruction of jet and shock layer flows, in *Proc. 21st Int. Symp. on Shock Waves, Great Keppel Island, Australia, July 20–25, 1997*, edited by Houwing *et al.*, Vol. 1, p. 435.

11. S. P. Sharma and S. Ruffin, Density measurements in an expanding flow using holographic interferometry, AIAA 92-0809.

12. A. Sasoh, K. Takayama, and T. Saito, A weak shock wave reflection over wedges, *Shock Waves* **2**, 277 (1992).

13. M. Sun and K. Takayama, A holographic interferometric study of shock wave focusing in a circular reflector, *Shock Waves* **6**, 323 (1996).

14. K. Takayama and O. Onodera, Shock wave propagation past circular cross sectional 90° bends, in *Proc. 14th Int. Symp. on Shock Tubes and Shock Waves, University of Sydney, New South Wales, Australia, 1983*, edited by Archer and Milton, p. 205.

15. K. Takayama and Z. Jiang, Shock wave reflection over wedges: A benchmark test for CFD and experiments, *Shock Waves* **7**, 191 (1997).

16. M. Takeda, H. Ina, and S. Kobayashi, Fourier transform method of fringe-pattern analysis for computer-based tomography and interferometry, *J. Opt. Soc. Am.* **22**, 824 (1981).

17. T. C. Tam, N. J. Brock, J. L. Cavolowsky, and L. A. Yates, Interferometry at the NASA–Ames hypervelocity free-flight aerodynamic facility, AIAA 91-0568.

18. Y. Tamura and K. Fujii, Visualization for computational fluid dynamics and the comparison with experiments, AIAA 90-3031.

19. A. Abe, *Shock Waves Discharged from the Open End of Shock Tubes*, Doctoral thesis, Graduate School of Tohoku University, Sendai, Japan (1991).

20. L. A. Yates, Images constructed from computed flowfield, *AIAA J.* **31**, 1877 (1993).

21. D. J. Bone, Fourier fringe analysis: The two-dimensional phase unwrapping problem, *Appl. Opt.* **30**, 3627 (1991).